Opto-Electronic Advances

Original Article

2018, Vol. 1, No. 5

DOI: 10.29026/oea.2018.180006

Demonstration of orbital angular momentum channel healing using a Fabry-Pérot cavity

Shibiao Wei[1], Dapeng Wang[1], Jiao Lin[1,2]*, Xiaocong Yuan[1]*

Orbital angular momentum (OAM) mode division provides a promising solution to push past the already exhausted available degrees of freedom available in conventional optical communications. Nevertheless, the practical deployment of OAM within a free-space optical (FSO) communications system is still hampered by a major challenge, namely that OAM-based FSO links are vulnerable to disturbances. Though several techniques, such as using various non-diffraction beams and multiple transmit–receive apertures, are proposed to alleviate the influence of disturbances, these techniques significantly reduce the performance with regard to combating single fading for spatial blockages of the laser beam by obstructions. In this work, we initially demonstrate that a Fabry-Pérot resonant cavity has the ability to implement OAM mode healing, even for a blocking percentage of over 50%. Consequently, the proposed method will expand the use of OAM in the FSO secure communications and quantum encryption fields.

Keywords: optical communication; orbital angular momentum; Fabry-Pérot cavity

Wei S B, Wang D P, Lin J, Yuan X C. Demonstration of orbital angular momentum channel healing using a Fabry-Pérot cavity. *Opto-Electronic Advances* **1**, 180006 (2018).

Introduction

Orbital angular momentum (OAM) is an intrinsic property of light and is identified by the transverse phase distribution of the wave front[1]. Generally, a vortex beam with a helical phase front, i.e., containing a phase term of $\exp(il\theta)$, carries an OAM quantum number of $l\hbar$ on each of its photons, where l is an unbounded integer indicating the topological charge, θ is the azimuthal angle, and $\hbar$ is Plank's constant. Laguerre-Gauss (LG) laser modes were the first to be identified as carrying OAM[2]. Akin to the spin angular momentum, also known as left- and right-handed circular polarization, OAM is a spatial (orbital) degree of freedom common to both classical and quantum waves[3]. The exotic property therefore enables OAM beams to have a range of unprecedented uses, e.g., for rotational Doppler metrology[4], optical spanners[5], quantum key distribution systems[6], high density data storage[7], astrophysics[8], and telecommunications[9–15], as well as finding applications in optical interferometers for the detection of gravitational waves[16,17]. In particular, the advantages of OAM have been explored in depth for high-capacity optical communication applications, because OAM can enhance the channel information capacity considerably owing to extensively diverse mode multiplexing without an increase in the spectral bandwidth[9–15]. In principle, various OAM modes are mutually orthogonal and consequently there is no interference or crosstalk between the multiplexing channels.

Despite free-space optical (FSO) communications systems that use OAM encoding/multiplexing technology having numerous advantages over conventional systems, such as being cost-effective, license-free, having access to a high bandwidth, and having been shown to be viable on a terabit/second scale in a laboratory environment[9–15,18], the widespread use of such systems still faces obstacles in complexes environments. In an open environment, intensity fluctuations caused by obstacles are introduced and become intractable challenges for FSO communications, causing a degradation of the systems' capacities.

To address these issues, the vast majority of prevalent solutions focus on finding ways of improving the laser source. Previous efforts that adopted non-diffraction beams (e.g. hypergeometric-Gaussian, Bessel-Gauss, and Hankel-Bessel beams) instead of *LG* beams were able to mitigate the effects of disturbances owing to their

[1]Nanophotonics Research Centre, Shenzhen Key Laboratory of Micro-Scale Optical Information Technology, Shenzhen University, Shenzhen 518060, China; [2]School of Engineering, RMIT University, Melbourne VIC 3000, Australia

* Correspondence: J Lin, E-mail: Jiao.Lin@osamember.org; X C Yuan, E-mail: xcyuan@szu.edu.cn

Received 13 April 2018; accepted 5 July 2018; accepted article preview online 6 July 2018

self-healing and partial coherence features[19–23]. The bit error rates of the transmitted signals carried by high order Bessel beams show smaller values and fluctuations[24]. Apart from the bit error rates, other statistical properties, such as the variance of the fluctuations of the OAM, M^2-factor, and the displacement error are less affected by these non-diffraction beams. Nevertheless, the above-mentioned disturbances were considered precisely within the Kolmogorov thin-phase regime, where the phase retardance and intensity arising from the local changes vary slightly and can therefore be approximated in a single plane[25]. Apart from these methods, the employment of multiple transmit–receive apertures in conjunction with error compensation also has the ability to combat single fading. However, the strict cornerstone of the co-alignment between the apertures prevents the promised diversity gains from being achieved. Though it is important to overcome the obstacle represented by OAM modal degradation during FSO communications, the above-described approaches are thoroughly incapable of working in the case of significant intensity or phase profile collapse, which might occur over long or more turbulent links. A strategy to enable OAM mode healing or restoration must thus be found to enable long-range secure communications or quantum encryption systems.

Methods

In this work, we proposed a method by which a Fabry-Pérot (FP) resonant cavity[26–29] enables the healing of collapsed OAM modes for the case of a prominent blockage over the spatial intensity of the beam profile. A variety of spatial blocking percentages of incoming OAM beams have been systematically investigated experimentally. It was found that a collapsed or undecipherable modal OAM beam can be picked up from a high-q resonator with a precise adjustment of the longitudinal cavity length. Note that the turbulence level is stronger than any other influence factors, such as random index variations in temperature, humidity, and atmospheric pressure. Intriguingly, this method presents a very promising way to heal a broken OAM beam, and is suitable for on-off keying and line-of-sight FSO communications[30].

The general solutions of the *LG* modes, the eigensolutions u_{pl} to the paraxial wave equation in cylindrical coordinates, have the form:

$$u_{pl}(r,\theta,z)=\frac{1}{\sqrt{1+z^2/z_{\mathrm{R}}^2}}[\frac{r\sqrt{2}}{w(z)}]^l L_p^l[\frac{2r^2}{w(z)^2}] \times\exp[\frac{-r^2}{w(z)^2}]\exp[\frac{-\mathrm{i}kr^2z}{2(z^2+z_{\mathrm{R}}^2)}]\exp(-\mathrm{i}l\theta) \times\exp[\mathrm{i}(2p+|l|+1)\psi(z)]\ , \quad (1)$$

here, L_p^l is the Laguerre-Gauss equation of order (p, l); p and l are the radial and azimuthal mode indexes, respectively; $w(z)$ is the standard definition of the beam waist; r, θ, and z are the radial, azimuthal, and longitudinal coordinates, respectively; and $z_{\mathrm{R}}=\pi w_0^2/\lambda$ is the Raleigh range of the beam. w_0 is the beam waist. When the beam propagates through the region around its focal point, the Gouy phase shift is given by the term $\psi(z)=\arctan(z/z_{\mathrm{R}})$. The mechanism for selecting different modes is reliant on the Gouy phase shift, i.e., the extra phase of any focusing beam within the cavity. This phenomenon, in which a propagating wave acquires a phase shift relative to a (theoretical) plane wave as it is focused by an optical system, was first observed in 1890[31]. For a FP cavity, a resonance only occurs when the phase shift from one side to the other is a multiple of π. For a fixed stable cavity, the total phase accumulated by an *LG* beam traveling between the two sides of the resonator (i.e., one side at z_1 and the other at z_2) can be written as

$$\phi(z_2-z_1)=kD-(2p+|l|+1)[\psi(z_2)-\psi(z_1)]. \quad (2)$$

This equation tells us that different *LG* modes will resonate with different cavity lengths D because of the influence of the Gouy phase[32]. The Gouy phase shift term related with the cavity parameters[33] was expressed as

$$\psi(z_2)-\psi(z_1)=\arccos(\pm g_1g_2) \quad (3)$$

where $g_{1,2}=1-D/R_{1,2}$, $R_{1,2}$ is the radius of curvature of the specified mirror and D is the mirror separation(known as cavity length). A cavity is stable in that case of $0\le g_1g_2\le 1$. The commercial scanning FP cavity used in our experiment was confocal ($D=R_1=R_2$) as such a confocal configuration would completely degenerate the response of the beams with odd or even coefficients $(2p+|l|+1)$. For different *LG* modes healing, the

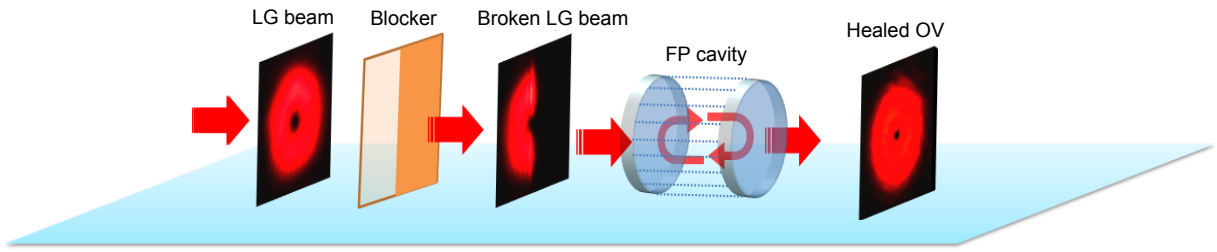

Fig. 1 | Conceptual diagram of a blocked LG beam healing system using a FP cavity. The blocked OV beam travels hundreds of times (depending on the *q* factor of the resonator) in the cavity when resonating. As the beam propagates back and forth, the blocked parts of the beam are 're-brightened'.

cavity length was extended (R_1=R_2=R<D<2R) to break the degeneration. Notably, when a broken beam (some parts of the beam had been blocked) propagated through the FP cavity, it was healed when it resonated in the cavity. This is because under resonance, the resonant beam will travel hundreds of times (depending on the q factor of the resonator) between the two mirrors. During this back and forth propagation, the blocked parts of the beam are 're-brightened', as shown in Fig. 1.

The schematic of the experimental setup is shown in Fig. 2. As the resonator is ultra-sensitive to the frequency of the incident beam, a frequency-stabilized He-Ne laser (Thorlabs HRS015B, vacuum wavelength of 632.991 nm) was used. An optical isolator was placed between the FP cavity and the He-Ne laser to prevent the reflected beam from propagating back to the laser cavity and breaking the stability of the laser beam. The beam then passed through a spatial filter with a 15-μm-diameter pinhole before being re-collimated to produce a higher quality Gaussian beam. A liquid-crystal-based spatial light modulator (SLM) (Boulder Nonlinear Systems, pixel pitch 15 μm × 15 μm fill factor 83.4%) was used to convert a well collimated linearly polarized beam into the LG beams. The filtered beam propagated through a 50/50 beam splitter (BS_1). One of the output beams was incident normally onto the SLM while the other beam was set to be an additional reference Gaussian beam for interference with the final output beam from the FP cavity. A phase-only interference pattern between a plane wave and a vortex beam of the desired topological charge was displayed on the SLM. The converted OAM beam was aligned to a scanning FP cavity, where the length of the cavity could be changed by a DC/AC controller. A modified commercial scanning FP cavity, Thorlabs SA200-5B, was used by changing the initial spacing of the two cavity mirrors from 50 mm to 70.06 mm to break the confocal configuration[31]. A thin lens with a focal length of 250 mm was used to achieve the beam size that matched the cavity. A sharp edge blocking-plate was placed before the FP cavity to block part of the incident beam. To obtain the interference pattern between the reference Gaussian beam and the transmitted beam from the FP cavity, a 50/50 beam splitter (BS_2) was used to combine them after the FP cavity. The transmitted signal was monitored via a photodiode (when an AC controller, Thorlabs SA-201, was used) or a charge-coupled device (CCD) camera (when a DC controller, Thorlabs MDT694B, was used).

Results

Here, the LG_0^1 mode (p=0, l=1) was used to demonstrate the healing ability of a broken beam passing though the FP cavity. The blocking-plate was mounted onto a one-dimensional translation stage to precisely control the unblocking percentage (based on the ratio of the unblocked part and the whole beam) of the incident beam. The pictures captured by a CCD camera in the first row of Fig. 3 show the intensity distribution of the incident beams to the FP cavity with different unblocking percentages from 100% to 10% of the beam's diameter. Compared with the random index variations in temperature, humidity and atmospheric pressure, this turbulence level is very strong. The distance between the CCD camera and the blocking-plate was about 10 cm, which caused some diffraction fringes. When the length of the FP cavity was set to cause LG_0^1 beam resonance, the incident beam traveled hundreds of times back and forth in the cavity. The second and third row of Fig. 3 show the intensity distributions of the transmitted beams and the interference patterns between the transmitted beam and the reference beam after the FP cavity. As Eq. (2) shown, the

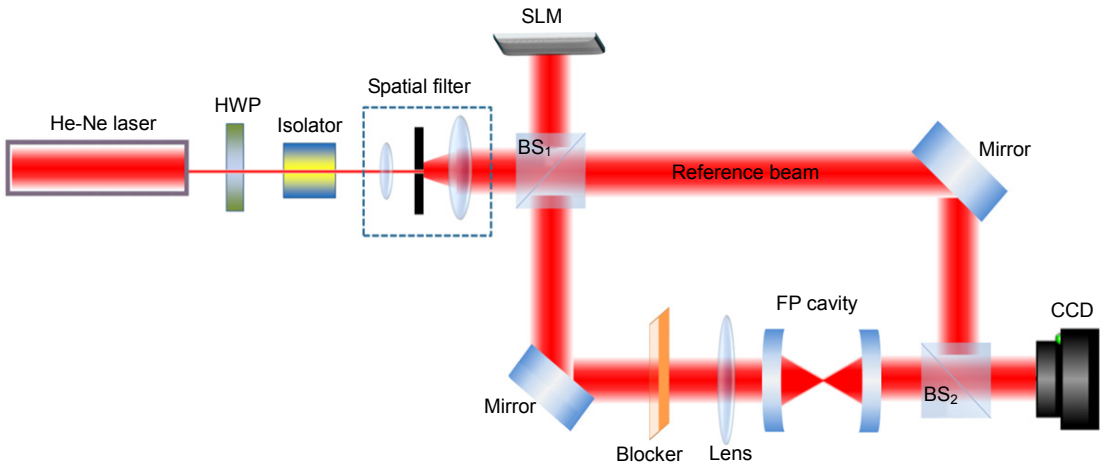

Fig. 2 | Illustration of the experimental setup. A linearly polarized beam from a He-Ne laser propagated through a half-wave plate (HWP) and an optical isolator before being spatially filtered. The filtered beam then traveled through a 50/50 beam splitter (BS_1), which provided a normal incidence beam onto the spatial light modulator and a reference Gaussian beam for generating the interference patterns. The OV beam was reflected from the first diffraction order of the SLM and mode-matched to the FP cavity using a thin lens with a focal length of 250 mm. A blocking-plate was then used to precisely control the blocking of the incident beam of the FP cavity. The transmitted light was monitored using either a CCD camera or a photodiode.

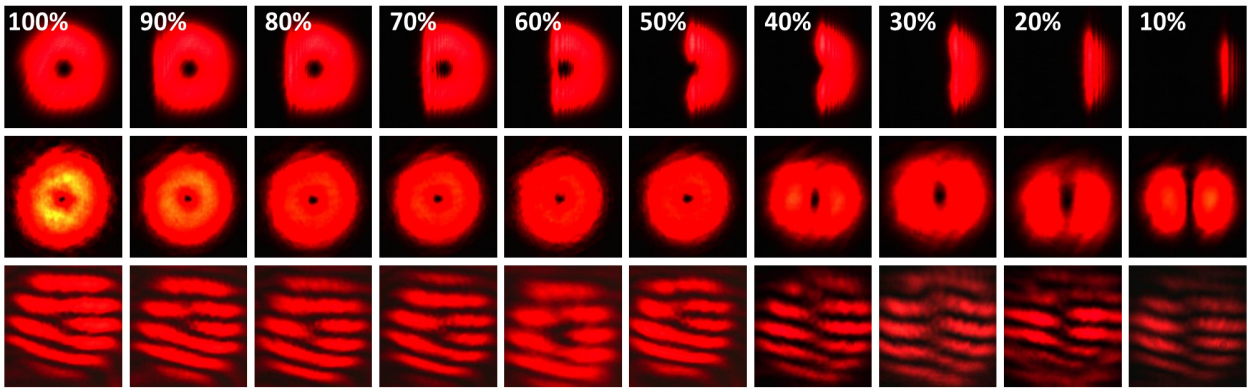

Fig. 3 | CCD captured experimental results. The first row shows the intensity distribution of the beams incident on the FP cavity with different unblocking percentages from 100% to 10%. The second row shows the intensity distribution of the transmitted light from the FP cavity with the resonant cavity length of the LG_0^1 beams. The third row shows the interference patterns between the transmitted light and the reference Gaussian beam.

degenerations of the same $N=|l|+2p$ would take place when the cavity length was fixed. The quality of the transmitted beam was degraded because the energy was reassigned to the degeneration *LG* states which also transmitted together with the original *LG* state. For instance of the LG_0^1 beam, the degeneration state is LG_0^{-1} and the mixed state shows a circular asymmetric feature of the intensity distribution. It is intractable to quantitatively distinguish the percentages of LG_0^1 beam and LG_0^{-1} beam. The Michelson contrast along a ring peak can be used to simply quantify the beam quality. When the blocking percentage was more than 50%, the transmitted beam would elapse the circular symmetric feature rapidly, resulting in two petal-pattern beams. So for LG_0^1 beam, it was healed to a circular symmetry donut intensity distribution when the unblocking percentage was 50% or higher. However, for the incident beams with an unblocking percentage below 50%, the transmitted beam became asymmetrical rapidly. The transmitted beams simultaneously carried LG_0^1 and LG_0^{-1} beams. The intensity of the LG_0^{-1} component increased when more light was blocked.

The scanning FP cavity's length could be actively tuned using a piezoelectric transducer controlled by an AC controller. A photodiode was used to detect the transmitted light from the FP cavity. The varied intensity distribution of the transmitted light was detected with an oscilloscope. A sharp peak appeared when the incident beam resonated in the FP cavity. By modifying the cavity length of $\lambda_c/2$ (where λ_c is the wavelength of the resonating beam in the cavity), another sharp peak was obtained because of the phase accumulation increment of π. Figure 4 clearly shows the intensity of the transmitted light changed over the course of the scanning time. The data from the oscilloscope with incident LG_0^1 beams with different unblocking percentages was normalized to the data of the LG_0^1 beam with a full donut intensity distribution. Though the intensities of the peaks decreased, the resonant positions of the LG_0^1 beam were not changed as the unblocking percentage of the incident beam decreased. However, some additional peaks appeared because of the mode crosstalk of the broken LG_0^1 beam that resulted in the energy reassignment to these peaks. For example, a beam with 50% unblocking illustrates this energy reassignment. In Fig. 5, the blue curve is the intensity of the transmitted light over the course of the scanning time. The inserted small pictures captured by the CCD camera are the intensity distribution of the main peaks when a DC controller was used to fix the length of the cavity. Figures 5(b) and 5(c) show the intensity distributions of two additional transmitted peaks between two adjusted LG_0^1 peaks. Those peaks are the LG_0^0 and LG_1^1 beams. This crosstalk was generated by the broken *LG* beam which was no more a pure *LG* beam with an integer topological charge. It is likely to be a *LG* beam with a fractional OAM state. In fact, the fractional OAM state could be regarded as the superposition of a number of *LG* states with integer index of *l* and *p*[34]. So a *LG* beam can be decomposed into several OAM states when it was blocked,

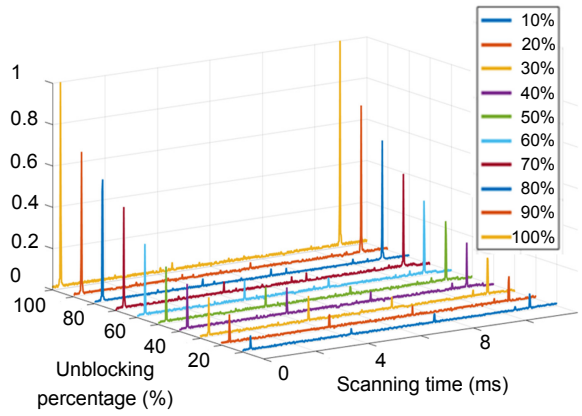

Fig. 4 | The various intensities of the transmitted light as a function of the change in the length of the Fabry-Pérot cavity as detected via a photodiode. When the unblocking percentage of the incident beams decreased, the intensity of the LG_0^1 peaks decreased because of the energy reassignment to other peaks.

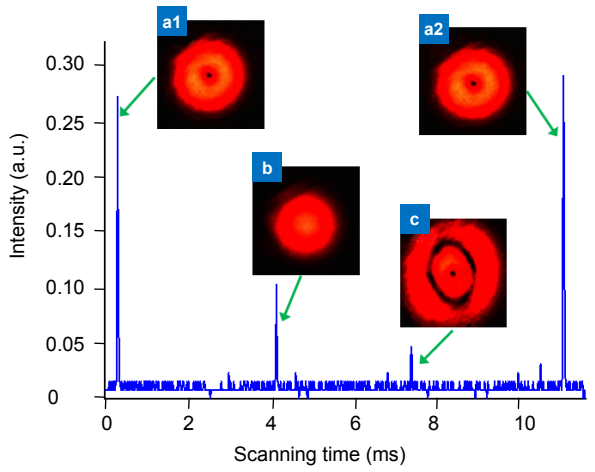

Fig. 5 | The transmitted curve of a 50% blocked LG_0^1 beam obtained from the scanning FP cavity and the intensity distributions of each main peak.

which was regarded as the energy reassigns in the mode crosstalk. Although the energy reassignment caused energy losses, the LG_0^1 beam was healed sufficiently, as shown in Figs. 5(a1) and 5(a2).

As Eqs. (2) and (3) shown, when a FP cavity was designed to break the degenerations of LG_0^l beams, in principle, the cavity had the capability to heal any *LG* states. For example, a 50% blocked LG_0^2 beam was sent to the FP cavity. The intensity distributions before and after the FP cavity were shown in Figs. 6(a) and 6(b). As Fig. 6(c) shown, the interference pattern between the transmitted light and the reference Gaussian beam indicated that the healed beam was LG_0^2 mode. However, for higher order *LG* beams (l >2), there are more degeneration modes with the same value of $N=|l|+2p$. It may degrade the beam quality of healed transmitted beam. For the open environment optical communications, the main turbulences, e.g., random index variations in temperature, humidity, and atmospheric pressure, will be much weaker than the turbulences caused by the 50% blocked beam. The degeneration modes crosstalk will be accordingly very weak as well.

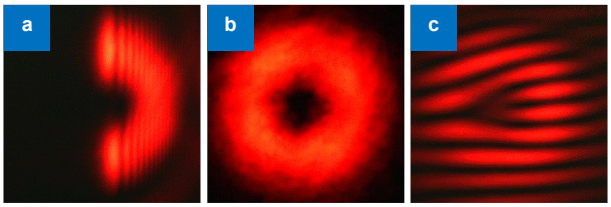

Fig. 6 | Experimental results for LG_0^2 beam. (**a**) The intensity distribution of the LG_0^2 beam incident on the FP cavity with unblocking percentages of 50%. (**b**) The intensity distribution of the transmitted light from the FP cavity with the resonant cavity length of the LG_0^2 beam. (**c**) The interference pattern between the transmitted light and the reference Gaussian beam.

Conclusions

In conclusion, we demonstrated a simple method to heal broken *LG* beams by using a FP resonator. LG_0^1 beams with different unblocking percentages were used as an example to demonstrate the healing capabilities of the resonator. The experimental results showed that the LG_0^1 beam could be completely healed when the unblocking percentage of the incident LG_0^1 beam was 50% or higher. However, for beams with an unblocking percentage of less than 50%, the transmitted light from the FP cavity simultaneously carried LG_0^1 and LG_0^{-1} beams because of the degeneration of these two beams when resonant conditions occurred. Furthermore, we discussed the energy reassignment phenomenon during the *LG* beams' healing, and analyzed the additional transmitted light from the FP cavity. In principle, this technique is not limited to healing the LG_0^1 beam, but is also suitable for healing other *LG* beams when resonating in a FP cavity. Our method offers a simple but powerful technique to heal broken *LG* channels in OAM open environment communications, which should increase the stability of free-space communication systems in a complicated disturbed environment.

References

1. Bliokh K Y, Rodríguez-Fortuño F J, Nori F, Zayats A V. Spin–orbit interactions of light. *Nat Photonics* **9**, 796–808 (2015).
2. Allen L, Beijersbergen M W, Spreeuw R J, Woerdman J P. Orbital angular momentum of light and the transformation of Laguerre-Gaussian laser modes. *Phys Rev A* **45**, 8185–8189 (1992).
3. Yao A M, Padgett M J. Orbital angular momentum: origins, behavior and applications. *Adv Opt Photonics* **3**, 161–204 (2011).
4. Belmonte A, Torres J P. Optical doppler shift with structured light. *Opt Lett* **36**, 4437–4439 (2011).
5. Lavery M P, Speirits F C, Barnett S M, Padgett M J. Detection of a spinning object using light's orbital angular momentum. *Science* **341**, 537–540 (2013).
6. Mirhosseini M, Magaña-Loaiza O S, O'Sullivan M N, Rodenburg B, Malik M *et al*. High-dimensional quantum cryptography with twisted light. *New J Phys* **17**, 033033 (2015).
7. Ren H, Li X, Zhang Q, Gu M. On-chip noninterference angular momentum multiplexing of broadband light. *Science* **352**, 805–809 (2016).
8. Berkhout G C, Beijersbergen M W. Method for probing the orbital angular momentum of optical vortices in electromagnetic waves from astronomical objects. *Phys Rev Lett* **101**, 100801 (2008).
9. Bozinovic N, Yue Y, Ren Y X, Tur M, Kristensen P *et al*. Terabit-scale orbital angular momentum mode division multiplexing in fibers. *Science* **340**, 1545–1548 (2013).
10. Lei T, Zhang M, Li Y R, Jia P, Liu G N *et al*. Massive individual orbital angular momentum channels for multiplexing enabled by Dammann gratings. *Light Sci Appl* **4**, e257 (2015).
11. Yan Y, Xie G D, Lavery M P J, Huang H, Ahmed N *et al*. High-capacity millimetre-wave communications with orbital angular momentum multiplexing. *Nat Commun* **5**, 4876 (2014).
12. Gibson G, Courtial J, Padgett M J, Vasnetsov M, Pas'Ko V *et al*.

Free-space information transfer using light beams carrying orbital angular momentum. *Opt Express* **12**, 5448–5456 (2004).
13. Lin J, Yuan X C, Tao S H, Burge R E. Multiplexing free-space optical signals using superimposed collinear orbital angular momentum states. *Appl Opt* **46**, 4680–4685 (2007).
14. Willner A E, Huang H, Yan Y, Ren Y, Ahmed N *et al*. Optical communications using orbital angular momentum beams. *Adv Opt Photonics* **7**, 66–106 (2015).
15. Wang J, Yang J Y, Fazal I M, Ahmed N, Yan Y *et al*. Terabit free-space data transmission employing orbital angular momentum multiplexing. *Nat Photonics* **6**, 488–496 (2012).
16. Bondarescu M, Thorne K S. New family of light beams and mirror shapes for future LIGO interferometers. *Phys Rev D* **74**, 082003 (2006).
17. Mours B, Tournefier E, Vinet J Y. Thermal noise reduction in interferometric gravitational wave antennas: using high order TEM modes. *Class Quantum Gravity* **23**, 5777–5784 (2006).
18. Malik M, O'Sullivan M, Rodenburg B, Mirhosseini M, Leach J *et al*. Influence of atmospheric turbulence on optical communications using orbital angular momentum for encoding. *Opt Express* **20**, 13195–13200 (2012).
19. Li Y, Zhang Y X. Oam mode of the hankel–bessel vortex beam in weak to strong turbulent link of marine-atmosphere. *Laser Phys* **27**, 045201 (2017).
20. Tyson R K. Bit-error rate for free-space adaptive optics laser communications. *J Opt Soc Am A Opt Image Sci Vis* **19**, 753–758 (2002).
21. Navidpour S M, Uysal M, Kavehrad M. Ber performance of free-space optical transmission with spatial diversity. *IEEE Trans Wireless Commun* **6**, 2813–2819 (2007).
22. Ma J, Jiang Y J, Tan L Y, Yu S Y, Du W H. Influence of beam wander on bit-error rate in a ground-to-satellite laser uplink communication system. *Opt Lett* **33**, 2611–2613 (2008).
23. Cheng M J, Guo L X, Li J T, Zhang Y X. Channel capacity of the oam-based free-space optical communication links with bessel–gauss beams in turbulent ocean. *IEEE Photonics J* **8**, 7901411 (2016).
24. Yuan Y S, Lei T, Li Z H, Li Y J, Gao S C *et al*. Beam wander relieved orbital angular momentum communication in turbulent atmosphere using bessel beams. *Sci Rep* **7**, 42276 (2017).
25. Lavery M P J, Peuntinger C, Günthner K, Banzer P, Elser D *et al*. Free-space propagation of high-dimensional structured optical fields in an urban environment. *Sci Adv* **3**, e1700552 (2017).
26. Abramovici A, Althouse W E, Drever R W P, Gürsel Y, Kawamura S *et al*. LIGO: the laser interferometer gravitational-wave observatory. *Science* **256**, 325–333 (1992).
27. Rüdiger A, Schilling R, Schnupp L, Winkler W, Billing H *et al*. A mode selector to suppress fluctuations in laser beam geometry. *J Mod Opt* **28**, 641–658 (1981).
28. de Graauw T, Haser L N, Beintema D A, Roelfsema P R, van Agthoven H *et al*. Observing with the ISO short-wavelength spectrometer. *Astrono Astrophys* **315**, L49–L54 (1996).
29. Jacquinot P. New developments in interference spectroscopy. *Rep Prog Phys* **23**, 267–312 (1960).
30. Sun X L, Djordjevic I B. Physical-layer security in orbital angular momentum multiplexing free-space optical communications. *IEEE Photonics J* **8**, 7901110 (2016).
31. Gouy L G. *Surune PropriÉTÉ Nouvelle Des Ondes Lumineuses* (Gauthier-Villars, 1890).
32. Wei S B, Earl S K, Yuan X C, Kou S S, Lin J. Active sorting of orbital angular momentum states of light with cascaded tunable resonators (2017); https://arxiv.org/abs/1704.01703.
33. Siegmann A E. *Lasers* (University Science Books, 1986).
34. Andrews D L, Babiker M, editors. *The Angular Momentum of Light*, 379–382 (Cambridge University Press, 2012).

Acknowledgements

This work is partially supported by the National Natural Science Foundation of China (11604219, 61675136, U701661, 61427819, 61138003, 61490712); the Leading talents of Guangdong province program (00201505); the Natural Science Foundation of Guangdong Province (2016A030312010); Science and Technology Innovation Commission of Shenzhen (KQTD2015071016560101) and Shenzhen Peacock Program (KQTD2017033011044403, KQTD 2017033011044403).

Competing interests

The authors declare no competing financial interests.